NUFFT-Based Interpolation in Backprojection Algorithms

Alfonso Breglia, Amedeo Capozzoli, *Member, IEEE*, Claudio Curcio, *Member, IEEE*, and Angelo Liseno

***Abstract*— We consider the interpolation problem associated with the back-projection (BP), fast BP (FBP), and fast factorized BP (FFBP) algorithms exploited in synthetic aperture radar (SAR). The 2-D interpolation required by FBP and FFBP must be properly performed to mitigate the effect of the truncation error and to achieve accurate results, and can be effectively performed by adopting 2-D nonuniform fast Fourier transform (NUFFT) routines.**

***Index Terms*— Synthetic aperture radar (SAR), computational complexity, interpolation.**

I. Introduction

THE back-projection (BP) algorithm is often used in synthetic aperture radar (SAR) since it does not involve approximations of the Green's function and is not limited to rectilinear trajectories [1]–[5]. However, BP is computationally demanding. Its burden is $P(N) + \mathcal{O}(N^2 \log N)$ for an $N \times N$ image, where $\mathcal{O}(N^2 \log N)$ accounts for the fast Fourier transform (FFT) step and $P(N)$ is a polynomial term associated with the interpolation between uniform and nonuniform grids [3]–[5]. Typical behaviors of $P(N)$ are $\mathcal{O}(N^4)$ or $\mathcal{O}(N^3)$ [6], [7].

Alternatives have been proposed to reduce its computational burden by sacrificing image quality in favor of computational complexity. They are based on a partitioning [8] or on a hierarchical partitioning of the aperture [9] according to the *divide et impera* strategy. So, the fast BP (FBP) [8] reduces the complexity of BP to $\mathcal{O}(N^{5/2})$, while the fast factorized BP (FFBP) scheme [9] achieves an $\mathcal{O}(N^2 \log N)$ complexity. However, domain decompositions or hierarchical domain decompositions are unavoidably associated with losses of accuracy due to the need of applying interpolations a larger number of times than BP. Accordingly, interpolation errors can cumulate, especially at the edges of the interpolation domains. Nevertheless, the total number of operations decrease, so a gain in computational complexity is achieved overall. The tradeoff between computational complexity and image quality has been faced by different authors, as, for example, Basu and Bresler [10].

BP has been recently improved to reduce its complexity while preserving accuracy [4], [5]. In fact, depending on the interpolation scheme, $P(N)$ or $\mathcal{O}(N^2 \log N)$ can be dominant and so the interpolator is crucial to favorably trading off accuracy and processing speed. To be effective, an interpolator should require information on the class of functions to interpolate as in the case of bandwidth information [11], [12]. In [4] and [5], 1-D nonuniform FFTs (NUFFTs) achieves a $\mathcal{O}(N^2 \log N)$ complexity and a very convenient tradeoff between complexity and accuracy. Furthermore, in FBP and FFBP, the aperture partitionings lead to the calculation of partial images which can be performed as in the BP. Finally, such partial images require 2-D interpolation stages [13] to combine them into common computational grids. Accordingly, effective interpolation is a fundamental step for either BP, or FBP or even FFBP.

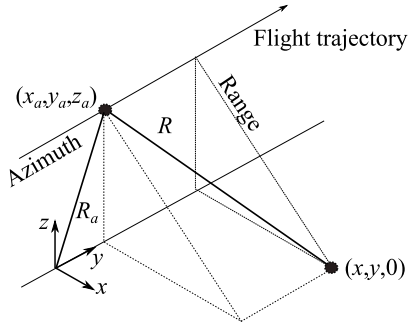

Fig. 1. Considered SAR geometry.

The aim of this letter is twofold: 1) underline that the computation of the partial images in FBP and FFBP can be performed using 1-D NUFFT routines as in BP [4], [5] and 2) show that the 2-D interpolations requested by FBP and FFBP can be accurately and quickly (reduced computational complexity) computed by 2-D NUFFTs. In other words, we substitute all the interpolation steps required by FBP and FFBP with NUFFT-based interpolations.

In Section II, we recall the 1-D NUFFT-based BP approach already developed in [4] and [5] since it is the building block for the computation of partial images in FBP and FFBP.

II. BP and Its NUFFT-Based Computation

The geometry is illustrated in Fig. 1. Here, a rectilinear flight trajectory is assumed for the sake of clarity, while, in Section V, this hypothesis will be removed. We use the following symbols: t—slow time; τ—fast time; c—light speed; $\underline{r}_a(t) = (x_a(t), y_a(t), z_a(t))$—flight trajectory; (x, y)—ground coordinates.

BP consists of approximating the ground reflectivity $\gamma(x, y)$ by $h(x, y)$ as [4], [5]

$$h(x, y) = \sum_n \int S(t_n, f) e^{j2\pi f \frac{2\Delta R(x,y,t_n)}{c}} df \tag{1}$$

Manuscript received December 30, 2019; revised February 14, 2020; accepted February 18, 2020. Date of publication August 12, 2020; date of current version November 24, 2021. *(Corresponding author: Amedeo Capozzoli.)*

The authors are with the Dipartimento di Ingegneria Elettrica e delle Tecnologie dell'Informazione, Università di Napoli Federico II, 80125 Napoli, Italy (e-mail: a.capozzoli@unina.it).

Digital Object Identifier 10.1109/LGRS.2020.3013444

where t_n is the slow-time instant at which the nth pulse illuminating the scene is sent, $S(t_n, f)$ is the nth signal after range compression of the raw data, f is the frequency, $R_a(t_n) = ||\underline{r}_a(t_n)||$, $R(x, y, t_n) = ||\underline{r} - \underline{r}_a(t_n)||$, $\Delta R(x, y, t_n) = R(x, y, t_n) - R_a(t_n)$, and $\underline{r} = (x, y, 0)$. Equation (1) holds under the start-and-hop approximation and when neglecting the antenna range-spreading loss is possible. In addition, the phase in (1) has been referred to $R_a(t_n)$ to ease the application of the NUFFT algorithm (see below).

On denoting by $s(t_n, \tau)$ the inverse Fourier transform of $S(t_n, f)$, then BP consists of computing (1) as

$$h(x, y) = \sum_n s\left(t_n, \frac{2\Delta R(x, y, t_n)}{c}\right). \tag{2}$$

Let us suppose the image grid to be the Cartesian grid $(x_i, y_k) = (i\Delta x, k\Delta y)$, Δx and Δy being the image sampling steps. For each value of n, the quantity

$$s\left(t_n, \frac{2\Delta R((x_i, y_k), t_n)}{c}\right) \tag{3}$$

is of interest. Assuming uniform sampling of $s(t_n, \tau)$ in τ leading to $s(t_n, \tau_p)$, where $\tau_p = p\Delta\tau$, $\Delta\tau = \alpha/(2BW)$ is the sampling step in time domain, BW is the bandwidth of the illuminating pulse, and $\alpha \leq 1$ is an oversampling factor, the term (3) can be computed by an Inverse Fast Fourier Transform (IFFT) of $S(t_n, f_q)$ to obtain $s(t_n, \tau_p)$ and a 1-D interpolation of $s(t_n, \tau_p)$ from the uniform grid τ_p to the nonuniform grid defined by $2\Delta R((x_i, y_k), t_n)/c$. It is noted that the above-mentioned sampling step $\Delta\tau$ accounts for a real-valued signal s, while twice the step would be needed when using a complex representation and when exploiting signal symmetries is possible.

In [4] and [5], it has been recognized that the integral in (1) amounts at calculating the quantity s in (3) as

$$\sum_q S(t_n, f_q) e^{j2\pi f_q \frac{2\Delta R((x_i, y_k), t_n)}{c}} \Delta f. \tag{4}$$

Expression (4) can be efficiently and effectively computed by using a 1-D NUFFT of nonequispaced results (NER) type [14]–[16], being the input sampling f_q regular, but the output sampling defined by $2\Delta R((x_i, y_k), t_n)/c$ irregular. Indeed, a 1-D NER-NUFFT fastly computes the following NER-type nonuniform discrete Fourier transform (NUDFT) relationship between $\{z_q\}_{q=-Q/2}^{q=Q/2-1}$ and $\{\hat{z}_p\}_{p=1}^{P}$ [14]:

$$\hat{z}_p = \sum_{q=-Q/2}^{Q/2-1} z_q e^{-j2\pi \frac{q}{Q} x_p}. \tag{5}$$

In (5), the output sampling locations x_p must belong to $[-P/2, P/2]$, so referencing the phase to $R_a(t_n)$ simplifies meeting this condition. In the case when $Q \sim P \sim N_s$, 1-D NUFFT scales as $\mathcal{O}(N_s \log N_s)$, so that it does not further burden BP. The above approach overcomes the computational burden of the exact inversion algorithm in [17]. A detailed analysis on the advantages of using NUFFTs against other schemes involving the use of FFTs + interpolation has been presented in [5]. The optimized NUFFT in [16] is capable to almost reach double precision accuracy with a computational speed practically equal to that of a standard FFT.

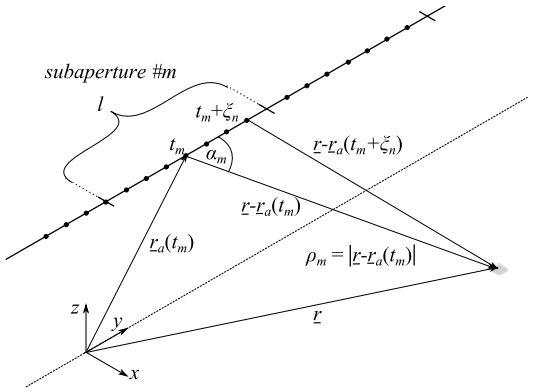

Fig. 2. Relevant geometry for the FBP algorithm.

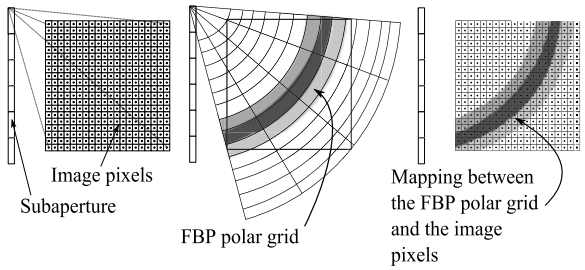

Fig. 3. FBP: Mapping between the image pixels and the generic PG.

III. FBP and 2-D NUFFT-Based Interpolations

FBP [8] divides the aperture into smaller subapertures of length l (Fig. 2), each associated with a partial image $h_m(x, y)$ [8]. The final image is obtained as a coherent superposition of the $h_m(x, y)$'s and each $h_m(x, y)$ can be efficiently and effectively computed according to the above BP scheme.

In FBP, the partial images can be computed in a fast way with a controllable degree of approximation. Indeed, on introducing a polar coordinate system $(\rho_m(x, y), \alpha_m(x, y))$ defined as in Fig. 2 [8] for the mth subaperture, the h_m's can be regarded as function of the polar coordinate systems, that is $h_m = h_m(\rho_m, \alpha_m)$. A uniform polar sampling grid $(\rho_{mh}, \alpha_{mr}) = (h\Delta\rho_m, r\Delta\alpha_m)$ can be chosen with $\Delta\rho_m \leq c/(2BW)$ and $\Delta\alpha_m \leq c/(2f_b l)$ [8], where f_b is the maximum frequency of the illuminating pulse. The angular resolution is inversely proportional to the subaperture length which means that keeping l small enables weakening the angular sampling requirements.

FBP requires a 2-D polar-to-Cartesian (P2C) interpolation from the uniform polar grid (PG) $(h\Delta\rho_m, r\Delta\alpha_m)$ onto the common Cartesian grid defined by the full aperture $(i\Delta x, k\Delta y)$ capable of avoiding the error accumulation [8]. The mapping between the generic PG and the final Cartesian grid is illustrated in Fig. 3. It is noted that the uniform Cartesian grid $(i\Delta x, k\Delta y)$ appears as a nonuniform grid in polar coordinates. Here, we exploit the *a priori* information on the bandlimitedness of the relevant functions to calculate and interpolate in one shot using a 2-D NER-NUFFT-based algorithm. Exploiting bandlimitedness enables, indeed, effective interpolation schemes with a very convenient tradeoff between accuracy and efficiency. The approach first transforms

$h_m(\rho_m, \alpha_m)$ from the polar (ρ_m, α_m) domain to the spectral $(k_{\rho_m}, k_{\alpha_m})$ domain

$$H_m(k_{\rho_m}, k_{\alpha_m}) = \iint h_m(\rho_m, \alpha_m) e^{-j(k_{\rho_m}\rho_m + k_{\alpha_m}\alpha_m)} d\rho_m d\alpha_m \tag{6}$$

and then transforms back to the (x, y) domain

$$h_m(\rho_m(x, y), \alpha_m(x, y)) = \frac{1}{4\pi^2} \times \iint H_m(k_{\rho_m}, k_{\alpha_m}) e^{j(k_{\rho_m}\rho_m(x,y) + k_{\alpha_m}\alpha_m(x,y))} \times dk_{\rho_m} dk_{\alpha_m}. \tag{7}$$

(See Fig. 4). The first step can be performed by standard FFT after having discretized (6) as

$$H_m(p\Delta k_{\rho_m}, q\Delta k_{\alpha_m}) = \sum_{h,r} h_{m_{hr}} e^{-jph\Delta k_{\rho_m}\Delta\rho_m} e^{-jqr\Delta k_{\alpha_m}\Delta\alpha_m} \Delta\rho_m \Delta\alpha_m \tag{8}$$

where the $h_{m_{hr}}$'s are the samples of $h_m(\rho_m, \alpha_m)$

$$\Delta k_{\rho_m}\Delta\rho_m = \frac{2\pi}{N_{\rho_m}} \quad \Delta k_{\alpha_m}\Delta\alpha_m = \frac{2\pi}{N_{\theta_m}} \tag{9}$$

and N_{ρ_m} and N_{α_m} are the number of samples of the $h_{m_{hr}}$'s in the variables ρ_m and α_m, respectively.

After having discretized (7) as

$$h_m(\rho_m(x_j, y_j), \alpha_m(x_j, y_j)) = \frac{1}{4\pi^2}\Delta k_{\rho_m}\Delta k_{\alpha_m} \sum_{p,q} H_m(p\Delta k_\rho, q\Delta k_\alpha) e^{jp\Delta k_{\rho_m}\rho_m(x_j,y_j)} \times e^{jq\Delta k_{\alpha_m}\alpha(x_j,y_j)} \tag{10}$$

the second step can be implemented by a 2-D NER-NUFFT. It is noted that, in (10), the Cartesian sampling points have been reorganized with a unique index j. It is also noted that, depending on the particular implementation, different kinds of spectral filtering (e.g., ramp filtering [9], [17]) can be needed.

IV. FFBP and 2-D NUFFT-Based Interpolations

FFBP [9] reduces the complexity over FBP trading off the complexity with accuracy. It recursively subdivides the subapertures into sub-subapertures through the organization of the subapertures in a tree-like structure. Subapertures of level $b-1$ are subdivided into sub-subapertures of level b. The hierarchical aperture partitioning terminates when a certain minimum aperture size is reached.

At first, FFBP requires the calculation of partial images associated with the lowest-level (smallest) subapertures which can be obtained by a BP scheme on a PG.

Afterward, climbing up the tree from level b to level $b-1$ requires a 2-D polar-to-polar (P2P) interpolation on grids that become closer and closer to the final polar one [9]. The mapping between the generic PG associated with subapertures of level b to the corresponding PG associated with subapertures of level $b-1$ is illustrated in Fig. 5. Notice that, since the origin of the involved PGs change, a uniform PG of level b appears to be nonuniform with respect to a uniform PG of level $b-1$ and vice versa.

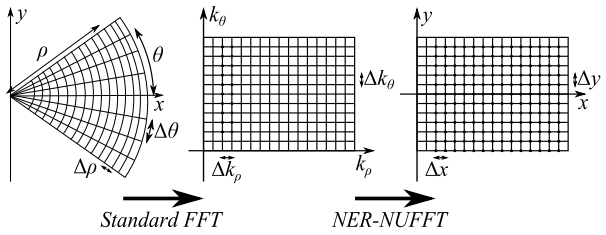

Fig. 4. FBP and FFBP: P2C interpolation.

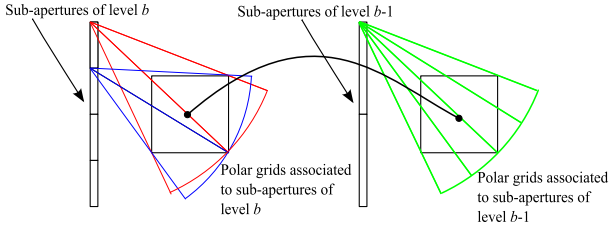

Fig. 5. FFBP: Mapping between the PGs associated with subapertures of level q and PGs associated with subapertures of level $q-1$.

At the last stage of the tree climbing, FFBP requires, just as FBP, 2-D P2C interpolation when resampling the partial images calculated in the uniform local polar coordinates associated with the subapertures of level 1 into the uniform Cartesian grid associated with the final image.

The P2P interpolation can be performed by a 2-D NUFFT-based two-step procedure which is again capable to avoid error accumulation. Let us denote by $(\rho_m^{(b-1)}, \alpha_m^{(b-1)})$ the polar coordinates of the mth subaperture of level $b-1$ and by $(\rho_j^{(b)}, \alpha_j^{(b)})$ the jth subaperture of level b contributing to the mth subaperture of level $b-1$. The problem at hand is interpolating the partial image $h_j^{(b)}$ from the uniform PG $(h'\Delta\rho_j^{(b)}, r'\Delta\alpha_j^{(b)})$ to the uniform PG $(h\Delta\rho_m^{(b-1)}, r\Delta\alpha_m^{(b-1)})$ to obtain $h_m^{(b-1)}$. Therefore, $h_j^{(b)}(h'\Delta\rho_j^{(b)}, r'\Delta\alpha_j^{(b)})$ is first transformed into the $(k_{\rho_j}, k_{\alpha_j})$ domain by a standard FFT and then transformed back to the (ρ_m, α_m) domain by a 2-D NER NUFFT as

$$h_{mj}^{(b-1)}\left(\rho_j\left(\rho_m^{(b)}, \alpha_m^{(b)}\right), \alpha_j\left(\rho_m^{(b)}, \alpha_m^{(b)}\right)\right) = \frac{1}{4\pi^2}\frac{\Delta k_{\rho_j}\Delta k_{\alpha_j}}{N_{\rho_j}N_{\alpha_j}} \sum_{pq} H_m(k_{\rho_{jp}}, k_{\alpha jq}) e^{jp\Delta k_{\rho_j}\rho_j\left(\rho_m^{(b)}, \alpha_m^{(b)}\right)} \times e^{jq\Delta k_{\alpha_j}\alpha_j\left(\rho_m^{(b)}, \alpha_m^{(b)}\right)} \tag{11}$$

where h_{mj} is the contribution of the jth subaperture of level b to the mth subaperture of level $b-1$ and $\rho_j(\rho_m^{(b)}, \alpha_m^{(b)})$ are the polar coordinates of the lower level as seen from the higher level.

Finally, the P2C interpolation can be performed as for FBP.

A. Spectral Windowing to Improve Accuracy

For the above 2-D NUFFT-based interpolations, the error arising from the truncation due to the finiteness of the 2-D spectral grid can be relevant. Accordingly, such interpolations must be properly improved by the use of a window function to control the truncation error and achieve accurate results.

Indeed, focusing the attention on the P2C interpolation, the result of the 2-D NUFFT-based scheme can be written as

$$\begin{aligned} h_m(\rho_m(x_j, y_j), \alpha_m(x_j, y_j)) &\simeq \Delta\rho_m \Delta\alpha_m \frac{K_{\rho_{m\max}} K_{\alpha_{m\max}}}{\pi^2} \\ &\times \sum_{h,r} h_{m_{hr}} \operatorname{sinc}(\pi K_{\rho_{m\max}}(\rho_m(x_j, y_j) - h\Delta\rho_m)) \\ &\times \operatorname{sinc}(\pi K_{\alpha_{m\max}}(\alpha_m(x_j, y_j) - r\Delta\alpha_m)) \end{aligned} \tag{12}$$

where $K_{\rho_{m\max}}$ and $K_{\alpha_{m\max}}$ provide the extent of the spectral region as defined by the FFT. Such series shows slow convergence related to the slow decrease of the *sinc* tails [18], [19]. A simple way to improve convergence is using appropriate windowing [18]–[20]. To illustrate this in a simple 1-D abstract case, consider a signal $a(t)$ bandlimited to B. The accelerated sampling series can be written as follows:

$$a(t) = \sum_{p=0}^{N-1} a(pT) g(t - pT) \operatorname{sinc}\left(\frac{t - pT}{T}\right) \tag{13}$$

where N is the number of samples of a, $BT < 1$, and $g(t)$ is a window introduced to mitigate the truncation problem [18]–[20]. It can be shown [20] that (13) can be calculated as

$$a(t) \simeq \frac{1}{N} \sum_{k=-k_g}^{k_g} A\left(\frac{k}{NT}\right) G_w\left(\frac{k}{NT}\right) e^{j2\pi \frac{kt}{NT}} \tag{14}$$

where A is the Fourier transform of a, $k_g = \operatorname{Int}(NB_gT/2)$, $\operatorname{Int}(x)$ is the closest integer to x, $B_g \leq 2/T - B$, and $G_w(f)$ is the spectrum of $g(t)\operatorname{sinc}(t/T)$. According to (10), (11), and (14), to reduce the truncation error, a window should be applied to the signal spectral samples before performing the 2-D NUFFT. In this letter, the approximate prolate (AP) spheroidal wave function is chosen [18]–[20] as window $g(t)$.

V. Numerical Results

We assess the performance of our interpolation approach against other interpolators typically employed in this framework, namely, nearest-neighbor, linear, cubic, and spline.

We have considered a 10.24 m $\times$ 10.24 m scene with 5 point scatterers located at $(0, 0)$, $(3, 0)$ m, $(-3, 0)$ m, $(0, 3)$ m, and $(0, -3)$ m. The range distance at the scene center is $R_0 = 10$ km, the depression angle is $\theta_d = \pi/4$, and the number of pulses [azimuth bins, or the number of n-samples in (4)] is 1024 for an overall integration angle of 2.9°. Center frequency and bandwidth are 9.6 GHz and 800 MHz, respectively, for an overall number of 256 frequency points (the number of q-samples in (4), that is the number of range bins of the original raw data). When computing the IFFT of $S(t_n, f_q)$, a zero padding of 8 is applied to improve the performance of the compared interpolators only and 2048 samples are used. The scene has been discretized into 77 $\times$ 64 pixels. A nonrectilinear flight trajectory has been accounted for with

$$\begin{cases} x(\sigma) = R_0 \cos(\theta_d)(1 + 0.001 * \cos(2\pi\sigma/L)) \\ y(\sigma) = \sigma \\ z(\sigma) = R_0 \sin(\theta_d)(1 + 0.002 * \cos(2\pi\sigma/L)) \end{cases} \tag{15}$$

where σ is the representation parameter and $L = 360$ m is the length of the synthetic aperture. The trajectory in (15) enables 10 m of deviation from a straight trajectory along the x-axis and 20 m along the z-axis. These deviations are assumed typical in airborne systems [21].

The reference image to compare with has been obtained by the BP approach when the 1-D NUDFT is computed by a 'brute-force' approach [5]. For the FBP case, the data have been partitioned into 32 subapertures. In the FFBP case, a 5 level hierarchy has been dealt with. The minimum subaperture size, namely, that referring to the deepest level 5 has been again 32. In both FBP and FFBP, a $2k_g + 1 = 29$ samples Knab window has been considered.

A notice is now in order concerning the number of operations involved in BP, FBP, and FFBP, and the number of approximations involved in the whole interpolation process. To this end, floating point operations are considered numerically exact so that the approximations in BP, FBP, and FFBP are due to the interpolations only.

Concerning the operations count, when passing from BP to FBP and finally to FFBP, the number of operations decreases. This has been already pointed out in [8] and [9].

Opposite to that, the number of approximations due to interpolation needed for the computations at (x, y) increases from BP to FBP and to FFBP and so interpolation errors can cumulate. To point this out, consider the case of N_{pulse} azimuth bins. In BP, we need N_{pulse} 1-D NUFFTs to form the image at (x, y): the number of interpolation approximations is thus N_{pulse}. In FBP, assume that the subapertures comprise N_{pulsesub} pulses, so that the number of subapertures is $N_{\text{pulse}}/N_{\text{pulsesub}}$. To form the image at (x, y), for each subaperture, we need N_{pulsesub} 1-D NUFFTs (in one shot, transform + interpolation) to compute the partial image in the PG. Furthermore, we need one 2-D NUFFT (interpolation only) to interpolate from the PG to the final Cartesian grid. For each subaperture, the number of interpolations is thus $N_{\text{pulsesub}} + 1$. Considering all the subapertures, the number of requested interpolations is $N_{\text{pulse}}/N_{\text{pulsesub}}(N_{\text{pulsesub}} + 1) > N_{\text{pulse}}$. Trivially, the number of approximations increases from FBP to FFBP.

In Fig. 6, the cut along the x-axis of the normalized differences between the reconstructions achieved by the considered interpolators and the reference image are depicted. Furthermore, in Table I, the percentage root mean square (rms) error between the reconstructions $h(x_j, y_j)$ and the reference image $h^{\text{REF}}(x_j, y_j)$ are reported, namely

$$\text{pRMS} = 100 * \sqrt{\frac{\sum_j |h(x_j, y_j) - h^{\text{REF}}(x_j, y_j)|^2}{\sum_j |h^{\text{REF}}(x_j, y_j)|^2}}. \tag{16}$$

The dramatic improvement of the considered interpolation scheme can be appreciated. Preserving the accuracy becomes more and more relevant when passing from BP, through FBP to FFBP since the number of requested interpolations increases. From Table I, the accuracy of FFBP using the proposed, NUFFT-based interpolation is comparable to that achieved by splines for the BP scheme.

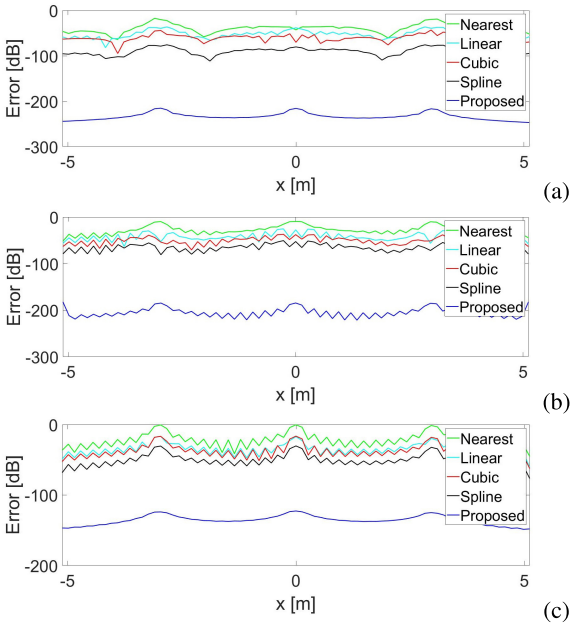

Fig. 6. Error with the reference image. (a) BP. (b) FBP. (c) FFBP.

TABLE I
RMS VALUES FOR THE DIFFERENT INTERPOLATION ALGORITHMS

Interpolation algorithm	BP	FBP	FFBP
Nearest	14.6%	40.9%	82.3%
Linear	2.00%	7.25%	23.6%
Cubic	1.14%	2.65%	13.7%
Spline	0.0237%	0.447%	3.32%
Proposed approach	$9.16 \cdot 10^{-13}\%$	$7.64 \cdot 10^{-8}\%$	$1.40 \cdot 10^{-4}\%$

VI. CONCLUSIONS AND FUTURE DEVELOPMENTS

We have shown how proper 2-D interpolations in FBP and FFBP can be effectively performed by adopting 2-D NUFFT routines, mitigating also the effect of the truncation error.

Notice that standard FFT is numerically exact, namely, exact within the limitations of floating point arithmetics. This notwithstanding, FFT is routinely employed in practical SAR applications. All the arising inaccuracies can be then ascribed to error sources different from FFT. The results show that with NUFFT things are similar. First, NUFFT is essentially numerically exact. Second, it has the same computational complexity of FFT. Furthermore, FFBP is not intrinsically poor in accuracy. Finally, the inaccuracies arising in practical applications are due to error sources different from interpolation. There is thus no point into skipping NUFFT.

An optimized NUFFT approach has been recently presented in [16], outperforming [14]. We now plan to extend the approach to parallel processing on graphics processing units [22].

REFERENCES

[1] J. C. Curlander and R. N. McDonough, *Synthetic Aperture Radar: Systems and Signal Processing*. New York, NY, USA: Wiley, 1991.

[2] R. Bamler, "A comparison of range-Doppler and wavenumber domain SAR focusing algorithms," *IEEE Trans. Geosci. Remote Sens.*, vol. 30, no. 4, pp. 706–713, Jul. 1992.

[3] L. A. Gorham and L. J. Moore, "SAR image formation toolbox for MATLAB," *Proc. SPIE*, vol. 7699, Apr. 2010, Art. no. 769906, doi: 10.1117/12.855375.

[4] A. Capozzoli, C. Curcio, A. Di Vico, and A. Liseno, "NUFFT- & GPU-based fast imaging of vegetation," *IEICE Trans. Commun.*, vol. E94-B, no. 7, pp. 2092–2103, 2011.

[5] A. Capozzoli, C. Curcio, and A. Liseno, "Fast GPU-based interpolation for SAR backprojection," *Prog. Electromagn. Res.*, vol. 133, pp. 259–283, 2013. [Online]. Available: http://www.jpier.org/PIER/pier.php?paper=12071909

[6] H. Choi and D. C. Munson, "Direct-Fourier reconstruction in tomography and synthetic aperture radar," *Int. J. Imag. Syst. Technol.*, vol. 9, no. 1, pp. 1–13, 1998.

[7] M. D. Desai and W. K. Jenkins, "Convolution backprojection image reconstruction for spotlight mode synthetic aperture radar," *IEEE Trans. Image Process.*, vol. 1, no. 4, pp. 505–517, Oct. 1992.

[8] A. F. Yegulalp, "Fast backprojection algorithm for synthetic aperture radar," in *Proc. IEEE Radar Conf. Radar Into Next Millennium*, Waltham, MA, USA, Apr. 1999, pp. 60–65.

[9] L. M. H. Ulander, H. Hellsten, and G. Stenstrom, "Synthetic-aperture radar processing using fast factorized back-projection," *IEEE Trans. Aerosp. Electron. Syst.*, vol. 39, no. 3, pp. 760–776, Jul. 2003.

[10] S. Basu and Y. Bresler, "$\mathcal{O}(N^2 log_2 N)$ filtered backprojection reconstruction algorithm for tomography," *IEEE Trans. Image Proc.*, vol. 9, no. 10, pp. 1760–1773, Oct. 2000.

[11] A. Kohlenberg, "Exact interpolation of band-limited functions," *J. Appl. Phys.*, vol. 24, no. 12, pp. 1432–1436, 1953.

[12] M. Soumekh, "Band-limited interpolation from unevenly spaced sampled data," *IEEE Trans. Acoust., Speech, Signal Process.*, vol. ASSP-36, no. 1, pp. 110–122, Jan. 1988.

[13] P.-O. Frölind and L. M. H. Ulander, "Evaluation of angular interpolation kernels in fast back-projection SAR processing," *IEE Proc.-Radar, Sonar Navigat.*, vol. 153, no. 3, pp. 243–249, Jun. 2006.

[14] K. Fourmont, "Non-equispaced fast Fourier transforms with applications to tomography," *J. Fourier Anal. Appl.*, vol. 9, no. 5, pp. 431–450, Sep. 2003.

[15] J. A. Fessler and B. P. Sutton, "Nonuniform fast Fourier transforms using min-max interpolation," *IEEE Trans. Signal Process.*, vol. 51, no. 2, pp. 560–574, Feb. 2003.

[16] A. Capozzoli, C. Curcio, and A. Liseno, "Optimized nonuniform FFTs and their application to array factor computation," *IEEE Trans. Antennas Propag.*, vol. 67, no. 6, pp. 3924–3938, Jun. 2019.

[17] L.-E. Andersson, "On the determination of a function from spherical averages," *SIAM J. Math. Anal.*, vol. 19, no. 1, pp. 214–232, Jan. 1988.

[18] J. Knab, "Interpolation of band-limited functions using the approximate prolate series (Corresp.)," *IEEE Trans. Inf. Theory*, vol. IT-25, no. 6, pp. 717–720, Nov. 1979.

[19] M. Migliaccio, F. Nunziata, F. Bruno, and F. Casu, "Knab sampling window for InSAR data interpolation," *IEEE Geosci. Remote Sens. Lett.*, vol. 4, no. 3, pp. 397–400, Jul. 2007.

[20] J. Selva, "Interpolation of bounded bandlimited signals and applications," *IEEE Trans. Signal Process.*, vol. 54, no. 11, pp. 4244–4260, Nov. 2006.

[21] A. Reigber and A. Moreira, "First demonstration of airborne SAR tomography using multibaseline L-band data," *IEEE Trans. Geosci. Remote Sens.*, vol. 38, no. 5, pp. 2142–2152, Sep. 2000.

[22] A. Breglia *et al.*, "GPU-accelerated fast and fast factorized SAR backprojections," in *Proc. 29th Int. Rev. Progr. Appl. Comput. Electromagn.*, Monterey, CA, USA, Mar. 2013, pp. 827–832.